NETWORKS AND HETEROGENEOUS MEDIA
©American Institute of Mathematical Sciences
Volume **4**, Number **3**, September **2009**

doi:10.3934/nhm.2009.4.431

pp. **431–451**

NON-OSCILLATORY CENTRAL SCHEMES FOR TRAFFIC FLOW MODELS WITH ARRHENIUS LOOK-AHEAD DYNAMICS

Alexander Kurganov and Anthony Polizzi

Mathematics Department, Tulane University
New Orleans, LA 70118, USA

(Communicated by Eitan Tadmor)

Abstract. We first develop non-oscillatory central schemes for a traffic flow model with Arrhenius look-ahead dynamics, proposed in [A. Sopasakis and M.A. Katsoulakis, SIAM J. Appl. Math., 66 (2006), pp. 921–944]. This model takes into account interactions of every vehicle with other vehicles ahead ("look-ahead" rule) and can be written as a one-dimensional scalar conservation law with a global flux. The proposed schemes are extensions of the non-oscillatory central schemes, which belong to a class of Godunov-type projection-evolution methods. In this framework, a solution, computed at a certain time, is first approximated by a piecewise polynomial function, which is then evolved to the next time level according to the integral form of the conservation law. Most Godunov-type schemes are based on upwinding, which requires solving (generalized) Riemann problems. However, no (approximate) Riemann problem solver is available for conservation laws with global fluxes. Therefore, central schemes, which are Riemann-problem-solver-free, are especially attractive for the studied traffic flow model. Our numerical experiments demonstrate high resolution, stability, and robustness of the proposed methods, which are used to numerically investigate both dispersive and smoothing effects of the global flux.

We also modify the model by Sopasakis and Katsoulakis by introducing a more realistic, linear interaction potential that takes into account the fact that a car's speed is affected more by nearby vehicles than distant (but still visible) ones. The central schemes are extended to the modified model. Our numerical studies clearly suggest that in the case of a good visibility, the new model yields solutions that seem to better correspond to reality.

1. **Introduction.** The main goal of this paper is to develop reliable and robust numerical methods for a new deterministic traffic flow model recently introduced in [29]. We also propose a more realistic modification of the model from [29] and study it using the designed schemes.

Traffic flow has been modeled by PDEs since the pioneering works [18] and [25]. The main idea in these models is to view cars as moving particles and to extend fluid dynamics approaches to traffic flows. We refer the reader to [7, 8, 9, 27, 30] for examples of gas-kinetic-type (mesoscopic) models and to [7, 22, 31] for some hydrodynamics-like (macroscopic) ones. Traffic flow has been also extensively modeled by stochastic differential equations (see [28, 29] and the references therein),

2000 *Mathematics Subject Classification.* Primary: 76M12, 35L65, 90B20; Secondary: 35L67.

Key words and phrases. traffic flow, scalar conservation law with a global flux, non-oscillatory central schemes, finite volume methods, Arrhenius look-ahead dynamics.

The first author is supported by NSF grants DMS-0310585 and DMS-0610430.

optimal velocity models (see, e.g., [1, 19, 24]), and cellular automaton models (see, e.g., [2, 20, 21]).

The simplest deterministic continuum traffic flow model is ([18, 25]):

$$u_t + f(u)_x = 0, \quad f(u) = uV(u), \quad V(u) = V_{\rm m}(1-u), \tag{1}$$

where $u(x,t)$ is a car density (measured in "cars per car length" so that $0 \le u \le 1$), $V_{\rm m}$ is the maximum possible speed, and $V(u)$ is the velocity function that is assumed to depend only on the density.

In [29], this model has been extended to a more realistic one by taking into account interactions with other vehicles ahead ("look-ahead" rule). This is done by treating vehicle movement as an asymmetric exclusion process (ASEP) on a periodic lattice representing a one-lane highway partitioned into N cells, $\mathcal{L} = \{1, 2, \ldots, N\}$. Vehicles are represented as a spin configuration σ, which is defined for each $x \in \mathcal{L}$ as

$$\sigma(x) = \begin{cases} 1, & \text{if a vehicle occupies cell } x, \\ 0, & \text{if the cell is empty,} \end{cases}$$

and offers the interpretation of the state of the system. Letting $\sigma = \{\sigma(x) : x \in \mathcal{L}\}$ gives a state variable within space $\{0,1\}^{\mathcal{L}}$. This approach models random dynamics in traffic, as the spin configuration is treated as a stochastic process. The effect cars have on each-other is represented in the interaction potential of vehicles in the ASEP model, in which the Arrhenius look-ahead dynamics is incorporated. This leads to a stochastic model presented and studied in [29].

It is also shown in [29] that under certain mild assumptions, the stochastic process describing traffic movement can be treated as deterministic. To this end, the fluctuations in $\{\sigma(x), x \in \mathcal{L}\}$ are approximated by the law of large numbers, and the resulting PDE is the following scalar conservation law with a global flux (see [29] for details):

$$u_t + F(u)_x = 0, \quad F(u) = V_{\rm m} u(1-u)\exp(-J \circ u), \tag{2}$$

where the contribution of short range interactions to the flux is modeled by the convolution

$$J \circ w(x) := \int_x^\infty J(y-x)w(y)\,dy. \tag{3}$$

In the first part of the paper, we follow [29] and consider a constant interaction potential

$$J(r) := \frac{1}{\gamma}\varphi\left(\frac{r}{\gamma}\right), \quad \varphi(r) := \begin{cases} 1, & 0 < r < 1, \\ 0, & \text{otherwise,} \end{cases}$$

that is,

$$J(r) = \begin{cases} 1/\gamma, & 0 < r < \gamma, \\ 0, & \text{otherwise,} \end{cases} \tag{4}$$

where γ is a positive constant proportional to the look-ahead distance. Introducing the anti-derivative, $U := \int_{-\infty}^x u(\xi,t)\,d\xi$, equation (2)–(3) can be rewritten as:

$$u_t + F(u,U)_x = 0, \quad F(u,U) = V_{\rm m} u(1-u)\exp\left(-\frac{U(x+\gamma)-U(x)}{\gamma}\right). \tag{5}$$

We are interested in developing accurate and reliable numerical methods for equation (5). Since this model is an extension of the simplest model (1), one may want to apply methods designed for scalar hyperbolic conservation laws to the global flux equation (5). The most popular methods are finite-volume methods (see, e.g.,

[4, 10, 16]) and, in particular, Godunov-type schemes. These schemes form a class of projection-evolution methods, in which a computed solution is first interpolated by a piecewise polynomial function and then evolved to the next time level according to the integral form of the conservation law. Godunov-type schemes are divided into two big classes: upwind and central. The evolution step of upwind schemes — both the original first-order Godunov scheme [5] and its higher-order extensions (see, e.g., [4, 10, 15, 16]) — are based on (approximate) solvers of the (generalized) Riemann problem. Unfortunately, no Riemann problem solvers are available for the global flux model (5), and it is therefore unclear how upwind schemes can be applied to it.

On the contrary, central schemes are based on the integration of conservation laws over the space-time control volumes that are selected so that each Riemann fan is entirely contained in its own control volume (this is achieved thanks to the finite speed of propagation). Thus, no (approximate) Riemann problem solver is needed, and therefore central schemes can be extended to problems for which the solution of the Riemann problem is unknown. The first-order Lax-Friedrichs (LxF) scheme [3, 14] is a prototype of central schemes. It is probably the most universal numerical method for time-dependent PDEs, but its resolution is quite low. The performance of the LxF scheme has been enhanced in [23], where the second-order central scheme — the Nessyahu-Tadmor (NT) scheme — was constructed by incorporating a second-order piecewise polynomial reconstruction into the LxF central framework.

The numerical dissipation present in the NT scheme can be further reduced if the contral volumes at every cell interface are taken to be proportional to the local speeds of propagation (rather than the global, as in the NT scheme). This has been done in [11, 12, 13], which introduce a new class of Godunov-type central schemes — the central-upwind (CU) schemes. The CU schemes do not use a staggered grid and admit a particularly simple semi-discrete form. Also, due to a smaller amount of numerical dissipation, the CU schemes can be successfully applied to problems requiring small time-steps and/or large time integration.

In this paper, we extend the NT and CU schemes to the conservation law with the global flux, (5). The new schemes, derived in §2.1 and §2.2, respectively, are applied to a number of test problems in §3. In Example 1, we demonstrate robustness and high resolution, achieved by the proposed method. We also perform a numerical convergence test, compare solutions of the equations with global and non-global fluxes, and study the dependence of numerical solutions on the look-ahead distance γ. Example 2 is designed to numerically study a dispersive effect of the global flux, which transforms a shock wave into a dispersive "wave package." Finally, in Example 3, we numerically investigate a breakdown phenomenon and discover that when γ is small, the smoothing effect of the global flux seems to be able to prevent the shock discontinuity formation.

At the end of the paper, we modify the model (2)–(4) by considering a more realistic, linear interaction potential

$$J(r)=\frac{1}{\gamma}\,\varphi\left(\frac{r}{\gamma}\right),\quad \varphi(r)=\begin{cases}2-2r, & 0<r<1,\\ 0, & \text{otherwise},\end{cases}$$

that is,

$$J(r)=\begin{cases}\dfrac{2}{\gamma}\left(1-\dfrac{r}{\gamma}\right), & 0<r<\gamma,\\ 0, & \text{otherwise}.\end{cases}\tag{6}$$

Compared with the original potential (4), the new one, (6), seems to be more realistic, especially in the case of large γ. Indeed, the cars that are visible to a driver but still far away should have less influence on the driver behavior than the cars that are nearby. In §4, we extend the NT and CU schemes to the new model and test them on a number of numerical examples with the same initial data as in §3. In the case of a good visibility (large γ), the obtained results are qualitatively different from the ones reported in §3.

2. Derivation of the central schemes.

In this section, we derive the staggered NT and the semi-discrete CU schemes for equation (5).

2.1. Staggered central scheme.

We first introduce the following notation: $x_\alpha = x_{\min} + (\alpha - 1/2)\Delta x$, $t^\beta = \beta\Delta t$, where Δx and Δt are small spatial and temporal scales assumed, for simplicity, to be constants throughout the computational domain $[x_{\min}, x_{\max}]$, divided into the cells $C_j := [x_{j-\frac{1}{2}}, x_{j+\frac{1}{2}}]$ so that

$$x_{\max} = x_{\min} + J\Delta x \quad \text{and} \quad [x_{\min}, x_{\max}] = \bigcup_{j=1}^{J} C_j.$$

Let us assume that at a certain time level $t = t^n$, the solution, realized by its cell averages,

$$\bar{u}_j^n := \frac{1}{\Delta x}\int\limits_{C_j} u(x, t^n)\,dx, \tag{7}$$

is available (we assume that the solution is compactly supported and that the computational domain $[x_{\min}, x_{\max}]$ is sufficiently large so that $\operatorname{supp} u(\cdot, t) \in [x_{\min}, x_{\max}]$ for all $t \in [0, T]$, where T is the final time). We then construct its piecewise linear interpolant

$$\widetilde{u}^n(x) := \bar{u}_j^n + s_j^n(x - x_j), \quad x \in C_j. \tag{8}$$

This reconstruction is (formally) second-order provided the slopes s_j^n are (at least) first-order approximations of the derivatives $u_x(x_j, t^n)$. A non-oscillatory nature of the interpolant (8) is achieved by computing the slopes with the help of a nonlinear limiter. A library of such limiters is available (see, e.g., [4, 10, 15, 16, 17, 23, 26]), and one can compute the numerical derivatives using one's favorite limiter. In our numerical experiments, we have used the generalized minmod reconstruction [15, 17, 23, 26] with:

$$s_j^n = \operatorname{minmod}\left(\theta\frac{\bar{u}_j^n - \bar{u}_{j-1}^n}{\Delta x}, \frac{\bar{u}_{j+1}^n - \bar{u}_{j-1}^n}{2\Delta x}, \theta\frac{\bar{u}_{j+1}^n - \bar{u}_j^n}{\Delta x}\right), \quad \theta \in [1, 2], \tag{9}$$

where the minmod function is defined as:

$$\operatorname{minmod}(z_1, z_2, ...) := \begin{cases} \min_j\{z_j\}, & \text{if } z_j > 0\ \forall j, \\ \max_j\{z_j\}, & \text{if } z_j < 0\ \forall j, \\ 0, & \text{otherwise,} \end{cases}$$

and the parameter θ can be used to control the amount of numerical viscosity present in the resulting scheme. It is well-known (see, e.g., [17]) that larger values of θ correspond to less dissipative but, in general, more oscillatory reconstructions. In our numerical experiments, we have used $\theta = 2$.

The reconstructed solution, $\widetilde{u}^n(x)$, is then evolved to the next time level $t = t^{n+1}$ by integrating equation (5) over the space-time control volumes $[x_j, x_{j+1}]\times[t^n, t^{n+1}]$, which, after division by Δx, results in:

$$\begin{aligned}\bar{u}^{n+1}_{j+\frac{1}{2}} &= \frac{1}{\Delta x}\int_{x_j}^{x_{j+1}} \widetilde{u}^n(x)\,dx \\ &\quad - \frac{1}{\Delta x}\int_{t^n}^{t^{n+1}} \Big[F(u(x_{j+1},t),U(x_{j+1},t)) - F(u(x_j,t),U(x_j,t))\Big]dt. \qquad (10)\end{aligned}$$

The first integral on the right-hand side (RHS) of (10) can be computed exactly. The flux integrals on the RHS of (10) should be computed using the (approximate) solution of the initial value problem (IVP) (5), (8) on the time interval $t \in (t^n, t^{n+1})$ with the initial data prescribed at $t = t^n$. Due to the finite speed of propagation, the solution of this IVP remains smooth at $x = x_j$ for all j provided the following CFL condition is satisfied:

$$\lambda a \le \frac{1}{2}, \quad \lambda := \frac{\Delta t}{\Delta x},$$

where a is the largest local speed that can be estimated by

$$a \le V_{\mathrm{m}} \max_{0\le u\le 1} |1-2u| = V_{\mathrm{m}}.$$

Therefore, the flux integrals in (10) can be "safely" approximated by the mid-point quadrature leading to

$$\begin{aligned}\bar{u}^{n+1}_{j+\frac{1}{2}} &= \frac{\bar{u}_j + \bar{u}_{j+1}}{2} + \frac{\Delta x}{8}(s^n_j - s^n_{j+1}) \\ &\quad - \lambda\Big[F(u(x_{j+1},t^{n+\frac{1}{2}}),U(x_{j+1},t^{n+\frac{1}{2}})) - F(u(x_j,t^{n+\frac{1}{2}}),U(x_j,t^{n+\frac{1}{2}}))\Big], \qquad (11)\end{aligned}$$

where the values of both the solution u and its antiderivative U at the intermediate time level $t = t^{n+\frac{1}{2}}$ can be approximated using the Taylor expansion, namely:

$$u(x_j,t^{n+\frac{1}{2}}) \approx \widetilde{u}^n(x_j) + \frac{\Delta t}{2}u_t(x_j,t^n), \quad U(x_j,t^{n+\frac{1}{2}}) \approx \widetilde{U}^n(x_j) + \frac{\Delta t}{2}U_t(x_j,t^n). \qquad (12)$$

In order to use these formulae, we need to provide the details on evaluating their RHSs. First, from equation (8) we have

$$\widetilde{u}^n(x_j) = \bar{u}^n_j,$$

and by integrating equation (8) from $x_{\min}$ to x we obtain the piecewise quadratic approximation of the antiderivative U:

$$\begin{aligned}\widetilde{U}^n(x) &= \int_{x_{\min}}^{x} \widetilde{u}^n(\xi)\,d\xi = \Delta x\sum_{i=0}^{j-1}\bar{u}^n_i + \int_{x_{j-\frac{1}{2}}}^{x} \widetilde{u}^n(\xi)\,d\xi \\ &= \Delta x\sum_{i=0}^{j-1}\bar{u}^n_i + \bar{u}^n_j(x - x_{j-\frac{1}{2}}) + \frac{s^n_j}{2}(x - x_{j-\frac{1}{2}})(x - x_{j+\frac{1}{2}}), \quad x \in C_j, \qquad (13)\end{aligned}$$

and, in particular, its point-values used in (12):

$$U^n_j := \widetilde{U}^n(x_j) = \Delta x\sum_{i=0}^{j-1}\bar{u}^n_i + \frac{\Delta x}{2}\bar{u}^n_j - \frac{(\Delta x)^2}{8}s^n_j. \qquad (14)$$

The time derivative u_t in (12) is evaluated with the help of equation (2):

$$u_t(x_j,t^n) = -F_x(u(x_j,t^n),U(x_j,t^n)), \tag{15}$$

and the space derivative F_x in (15) is computed using the minmod limiter:

$$F_x(u(x_j,t^n),U(x_j,t^n)) \;=\; \text{minmod}\left(\theta\,\frac{F(\bar{u}^n_j,U^n_j)-F(\bar{u}^n_{j-1},U^n_{j-1})}{\Delta x},\right.$$
$$\left.\frac{F(\bar{u}^n_{j+1},U^n_{j+1})-F(\bar{u}^n_{j-1},U^n_{j-1})}{2\Delta x},\;\theta\,\frac{F(\bar{u}^n_{j+1},U^n_{j+1})-F(\bar{u}^n_j,U^n_j)}{\Delta x}\right). \tag{16}$$

Finally, we integrate equation (15) with respect to x to obtain

$$U_t(x_j,t^n) = -F(u(x_j,t^n),U(x_j,t^n)) = -F(\bar{u}^n_j,U^n_j), \tag{17}$$

needed to complete the evaluation of u and U at the intermediate time level in (12).

Remark 1. Notice that a global approximation of U at time level t^n, given by (13), allows one to easily compute the global flux

$$F(\bar{u}^n_j,U^n_j) = V_{\rm m}\bar{u}^n_j(1-\bar{u}^n_j)\exp\left(-\frac{\widetilde{U}^n(x_j+\gamma)-\widetilde{U}^n(x_j)}{\gamma}\right),$$

even if $x_j+\gamma$ is not a grid node.

Remark 2. In practice, it is convenient to compute the point values of U^n_j recursively, that is, replacing (14) with:

$$U^n_j = U^n_{j-1}+\frac{\Delta x}{2}(\bar{u}^n_{j-1}+\bar{u}^n_j)+\frac{(\Delta x)^2}{8}(s^n_{j-1}-s^n_j).$$

Remark 3. The obtained second-order NT scheme for (5) is given by (11), (8)–(9), (12)–(17). It reduces to the first-order staggered LxF scheme if all the slopes are set to zero and the mid-point quadrature, used in the evaluation of the flux integrals in (10), is replaced with the left-sided rule. The resulting first-order scheme is:

$$\bar{u}^{n+1}_{j+\frac12} = \frac{\bar{u}_j+\bar{u}_{j+1}}{2}-\lambda\Big[F(u^n_{j+1},U^n_{j+1})-F(u^n_j,U^n_j)\Big].$$

Remark 4. Since the derived schemes use alternating, staggered grids, one has to distinguish between the "odd" and "even" time steps. The formulae (11), (8)–(9), (12)–(17) describe the "odd" steps. The "even" steps are obtained by shifting the indexes in the aforementioned equations by $\frac12$. Obviously, the computational domain should be extended by $\frac{\Delta x}{2}$ from both sides at every "even" step. This requires a careful implementation of the given boundary conditions. In our numerical examples, the solution was constant at the edges of the computational domain so that we used these constant values at the computational cells near the boundary.

2.2. **Semi-discrete central-upwind scheme.** We now proceed with the development of the CU scheme for equation (5). Equipped with the NT-type evolution operator for piecewise linear functions, which was derived in §2.1, we can simply follow the derivation of the fully discrete CU scheme carried out in [11]. Assume that a piecewise linear approximation of the solution is available at a certain time level t^n. We first construct non-uniform space-time control volumes, the sizes of which depend on the one-sided local speeds of propagation (the Riemann fans appearing at cell interfaces are always contained inside the control volumes). We then evolve the solution to the next time level using the NT technique, that is, without (approximately) solving a generalized Riemann problem. Finally, we project the

obtained solution back onto the original grid (see [11] for details). The only missing component is an estimate of the local speeds, which, for a scalar conservation law with a nonglobal flux $f(u)$, are computed using $f'(u)$, see [11]. For a global flux function, it may be not so easy to estimate the local speeds. However, the flux (5) contains the global exponential factor, which is nonnegative and always smaller than 1. Therefore, the upper/lower bounds for the right/left-sided local speeds for equation (5) are

$$a^+_{j+\frac12}=\max(1-2u^+_{j+\frac12},1-2u^-_{j+\frac12},0),\quad a^-_{j+\frac12}=\min(1-2u^+_{j+\frac12},1-2u^-_{j+\frac12},0), \tag{18}$$

where, $u^+_{j+\frac12}$ and $u^-_{j+\frac12}$ are the right- and left-sided values of the piecewise linear interpolant (8), respectively:

$$u^+_{j+\frac12}=\bar u^n_{j+1}-\frac{\Delta x}{2}s^n_{j+1},\quad u^-_{j+\frac12}=\bar u^n_j+\frac{\Delta x}{2}s^n_j. \tag{19}$$

Notice that having the upper and lower bounds on the local speeds is enough to ensure that all possibly nonsmooth nonlinear waves will remain inside the corresponding control volumes.

We then pass to the semi-discrete limit as $\Delta t\to 0$ along the lines of [11] and obtain the semi-discrete CU scheme for (5):

$$\frac{d}{dt}\bar u_j(t)=-\frac{H_{j+\frac12}-H_{j-\frac12}}{\Delta x}, \tag{20}$$

where the numerical flux $H_{j+\frac12}$ is given by

$$\begin{aligned}H_{j+\frac12}\ :=\ &\frac{a^+_{j+\frac12}F(u^-_{j+\frac12},U_{j+\frac12})-a^-_{j+\frac12}F(u^+_{j+\frac12},U_{j+\frac12})}{a^+_{j+\frac12}-a^-_{j+\frac12}}\\ &+\ a^+_{j+\frac12}a^-_{j+\frac12}\left[\frac{u^+_{j+\frac12}-u^-_{j+\frac12}}{a^+_{j+\frac12}-a^-_{j+\frac12}}-q_{j+\frac12}\right].\end{aligned} \tag{21}$$

Here, the built-in "anti-diffusion" term is

$$q_{j+\frac12}=\operatorname{minmod}\left(\frac{u^+_{j+\frac12}-u^{\rm int}_{j+\frac12}}{a^+_{j+\frac12}-a^-_{j+\frac12}},\frac{u^{\rm int}_{j+\frac12}-u^-_{j+\frac12}}{a^+_{j+\frac12}-a^-_{j+\frac12}}\right), \tag{22}$$

where the intermediate value $u^{\rm int}_{j+\frac12}$ is

$$u^{\rm int}_{j+\frac12}=\frac{a^+_{j+\frac12}u^+_{j+\frac12}-a^-_{j+\frac12}u^-_{j+\frac12}-\Big\{F(u^+_{j+\frac12},U_{j+\frac12})-F(u^-_{j+\frac12},U_{j+\frac12})\Big\}}{a^+_{j+\frac12}-a^-_{j+\frac12}}. \tag{23}$$

Formulae (21)–(23) are almost identical to the corresponding formulae for conservation laws with nonglobal fluxes (compare (21)–(23) with (3.3)–(3.5) in [11]). The only difference is in the dependence of the flux function F on $U_{j+\frac12}$, which is calculated using (19) and $\widetilde U$ (given by (13)):

$$F(u^\pm_{j+\frac12},U_{j+\frac12}):=V_{\rm m}u^\pm_{j+\frac12}(1-u^\pm_{j+\frac12})\exp\left(-\frac{\widetilde U(x_{j+\frac12}+\gamma)-\widetilde U(x_{j+\frac12})}{\gamma}\right).$$

Notice that in the semi-discrete formulation above, the cell averages, (7), the slopes, (9), the piecewise quadratic antiderivative (13), and all quantities in (21) are functions of time t, which is continuous at this stage. To obtain a fully discrete

scheme one has to discretize the ODE system (20) using a stable and sufficiently accurate ODE solver. In all numerical experiments, we have used the third-order strong stability preserving (SSP) Runge-Kutta method, see [6].

3. **Numerical examples.** In this section, we demonstrate the performance of the proposed central schemes for equation (5) on a number of test problems. In all numerical examples, the CFL number is 0.475, $V_{\mathrm{m}} = 4$, and the computational domain is taken large enough so that no waves reach its boundary within the final computational time.

Example 1—red light traffic. We consider equation (5) with different γ's subject to the following initial data:

$$u(x,0) = \begin{cases} 1, & 4 < x < 6, \\ 0, & \text{otherwise.} \end{cases} \tag{24}$$

This corresponds to a situation in which the traffic light is located at $x = 6$ and it is turned from red to green at the initial time moment.

We apply the proposed central schemes to the IVP (5), (24) and compute its solutions for different values of γ at time $t = 1$. We first fix $\gamma = 1$ and study the behavior of the VT and CU schemes. The solutions, computed on two uniform grids with $\Delta x = 1/5$ and $\Delta x = 1/10$, together with the reference solution, obtained by the CU scheme on a much finer uniform mesh with $\Delta x = 1/400$, are plotted in Figure 1. The resolution of the shock, achieved by the CU scheme, is slightly better than the one obtained by the NT scheme. The numerical convergence of the CU scheme is demonstrated in Figure 2: the mesh is further refined to $\Delta x = 1/20$ and $\Delta x = 1/40$, and the solution seems to converge to the reference solution. We note that due to the numerical diffusion, there are nonzero densities behind the shock (look at the area $x \in [3.9, 4]$ in Figure 2 (right)). This corresponds to (unphysical) backward movement of the cars. One can also see that as the mesh is further refined, no backward moving cars appear in the computed solution.

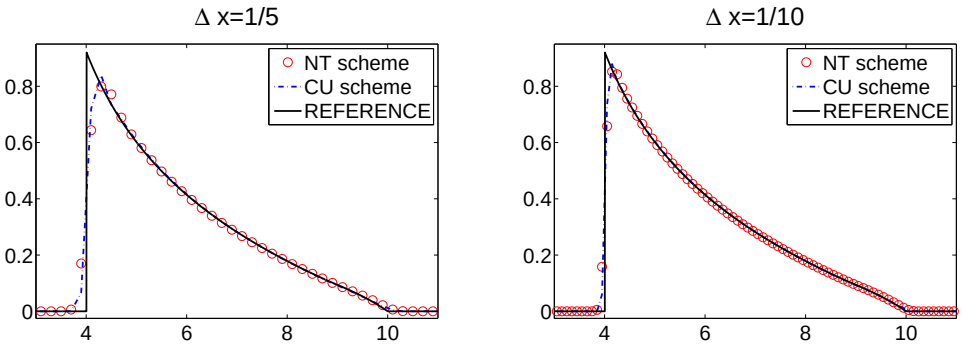

FIGURE 1. Numerical solutions of the IVP (5), (24) obtained by the NT and CU schemes on two different uniform grids

We also study the experimental convergence rate of the proposed schemes in the L^1-norm (the reference solution here has been computed by the CU scheme on a uniform grid with $\Delta x = 1/800$). The obtained results are reported in Table 1.

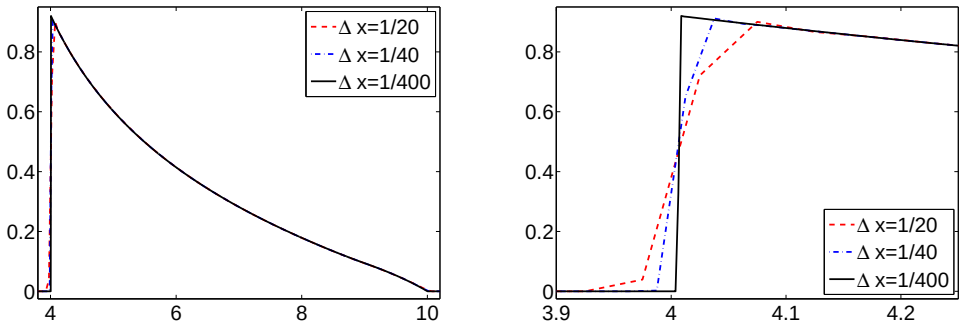

FIGURE 2. Numerical solutions of the IVP (5), (24) obtained by the CU scheme on two finer uniform grids (left); zoom at the shock area (right)

Δx	NT Scheme		CU Scheme	
	L^1-error	Rate	L^1-error	Rate
1/10	2.30e-02	–	1.19e-02	–
1/20	9.55e-03	1.27	4.12e-03	1.53
1/40	3.39e-03	1.49	8.84e-03	2.22
1/80	9.79e-04	1.79	3.29e-04	1.43

TABLE 1. L^1-errors and experimental convergence rates.

We then compare the computed solutions of the IVP (5), (24) and of a similar problem, but with non-global flux: (1), (24). Both solutions are obtained by the NT scheme on the same uniform mesh with $\Delta x = 1/20$. The solutions are shown in Figure 3 (left). One can clearly see the effect of the global flux that models the look-ahead dynamics. The effect is more prominent at the back end of the wave: the density wave corresponding to the global case clearly lags behind that of the non-global one. This can be explained by the awareness of traffic ahead. At the same time, since the interaction potentials vanish for vehicles at the front of the wave, the global and non-global solutions are almost identical there. To clarify the look-ahead effect, we show the global and non-global fluxes, $F(u, U)$ and $f(u)$, at time $t = 1$ (see Figure 3 (right)). As one can see, the difference between the fluxes is almost zero near $x = 10$ and it is largest at the back end of the wave. Notice the effect of the numerical diffusion: it smears u and, as a result, leads to an oscillatory behavior of the fluxes near the shock.

We finally demonstrate the dependence of the computed solution on the look-ahead distance γ. The solutions, obtained by the NT scheme for $\gamma = 0.1$, 0.2, 0.5, 1, and on the same uniform grid with $\Delta x = 1/40$ are presented in Figure 4. As one can clearly see there, the dependence on γ is significant: as γ decreases, the drivers can see less, that is, their sensitivity to interaction is lowered and the original traffic jam dissipates more slowly. On the contrary, when γ is very large, the effect of the global flux is negligibly small. In this context, it is instructive to look at the formal limits of the global flux in (5) as $\gamma \to \infty$ and $\gamma \to 0$. Clearly, when $\gamma \to \infty$ the

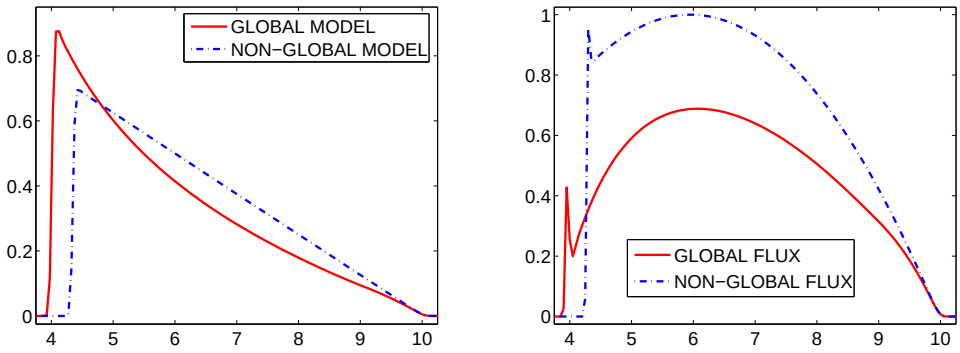

FIGURE 3. An impact of the look-ahead dynamics: numerical solutions of the global, (5), (24), and non-global, (1), (24), red light traffic models (left) and the corresponding fluxes (right)

global factor $\exp\left(-\frac{U(x+\gamma)-U(x)}{\gamma}\right) \to 1$ assuming the total number of cars on the freeway is bounded. Therefore,

$$F(u,U) \longrightarrow f(u) = V_{\rm m}u(1-u) \text{ as } \gamma \to \infty,$$

that is, the global model reduces to the original, non-global one. On the other hand, when $\gamma \to 0$, one has $\left(\frac{U(x+\gamma)-U(x)}{\gamma}\right) \to U_x(x) = u(x)$ and thus,

$$F(u,U) \longrightarrow f(u)e^{-u} = V_{\rm m}u(1-u)e^{-u} \text{ as } \gamma \to 0. \tag{25}$$

The factor e^{-u} is a "slow down" factor in the limiting low visibility case.

Example 2—traffic jam on a busy freeway. In the second example, we consider a different initial car density distribution:

$$u(x,0) = \begin{cases} 1, & 16 < x < 18, \\ 0.75, & \text{otherwise}, \end{cases} \tag{26}$$

and study the behavior of the solutions of the IVP (5), (26) for different γ's. Our numerical experiments clearly demonstrate convergence of the computed solutions as the grid is refined. We therefore omit the numerical convergence demonstration. All of the results presented in this example were obtained with the NT and CU schemes on one particular uniform grid with $\Delta x = 1/40$ (except the last figure, where the smoothness of the solution is numerically investigated using finer grids).

The dispersive effect, which could have been observed in Example 1, becomes much more prominent here since the waves are moving in the direction opposite to the vehicles' velocity. Even in the case of a relatively large $\gamma = 10$, the solution of the IVP (5), (26) (Figure 6) is significantly different from the solution of the corresponding IVP with a non-global flux (1), (26) (Figure 5). We then take a smaller $\gamma = 5$ and obtain quite similar solutions, though with dispersive waves meeting by time $t = 10$, see Figure 7.

We further decrease γ and discover a very interesting behavior of the solution. The results for $\gamma = 3$ are plotted in Figure 8 (note that the x-scaling is different in this figure from that used in Figures 5–7). Even though the waves are still initially separated, the larger waves catch the smaller ones much faster, forming a

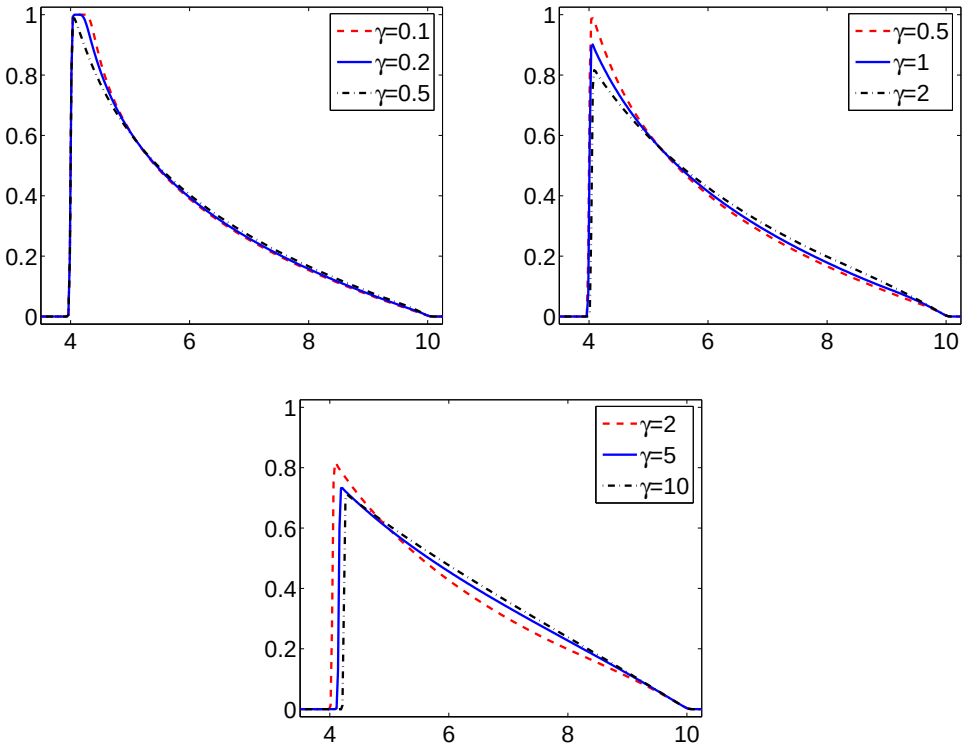

FIGURE 4. Dependence of the solution of the IVP (5), (24) on γ

dispersive "wave package" at about $t = 3$. When the look-ahead distance reduces to $\gamma = 1$, no separate waves are formed, but a dispersive "wave package" develops immediately and later transforms into a single wave, see Figure 9 (notice that the x-scaling has been changed once again). When γ is reduced to 0.5, the dispersive effect can be observed at small times only (Figure 10), and for even smaller $\gamma = 0.1$, no dispersive effect can be observed (Figure 11). In the latter case, the global flux leads to a certain smoothing effect though our fine mesh calculations suggest that the solution still contains a sub-shock at the left edge (front) of the wave, see Figure 12.

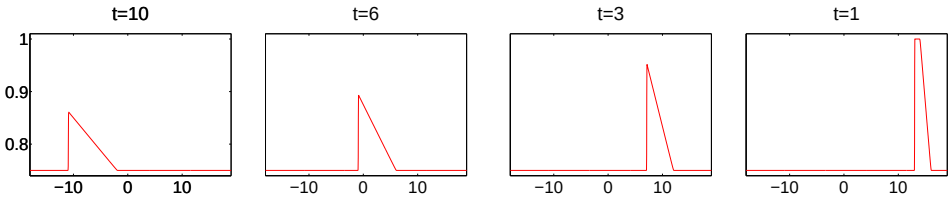

FIGURE 5. Time evolution (from right to left) of the solution of (1), (26)

Example 3—numerical breakdown study. Our final example is devoted to the numerical investigation of the smoothing effect of the global flux. As shown in Example

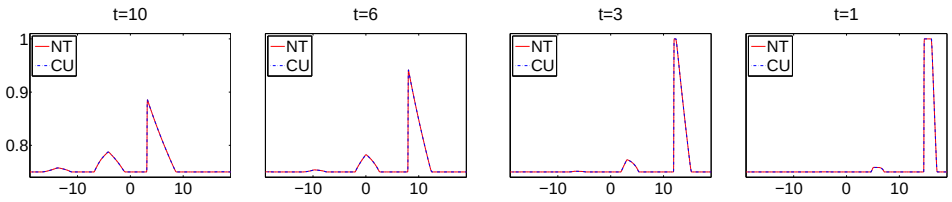

FIGURE 6. Time evolution (from right to left) of the solution of (5), (26) with $\gamma = 10$

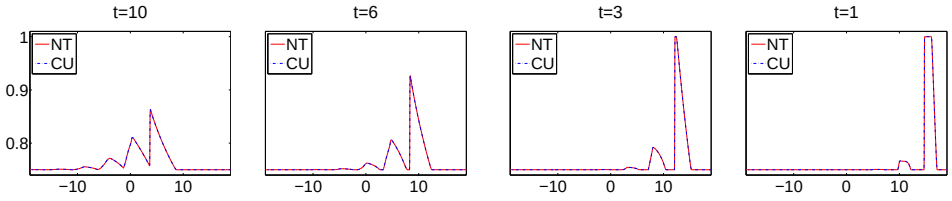

FIGURE 7. Same as in Figure 6 but with $\gamma = 5$

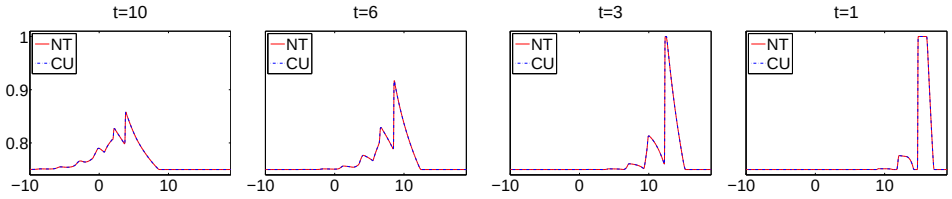

FIGURE 8. Same as in Figures 6–7 but with $\gamma = 3$

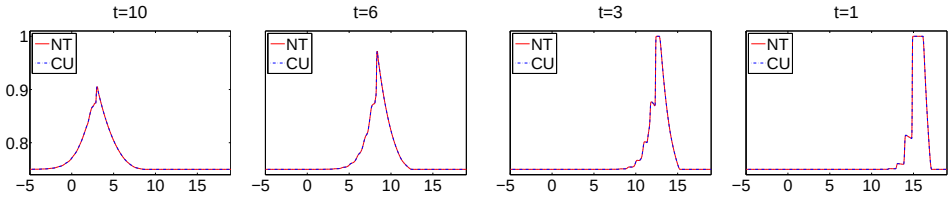

FIGURE 9. Same as in Figures 6–8 but with $\gamma = 1$

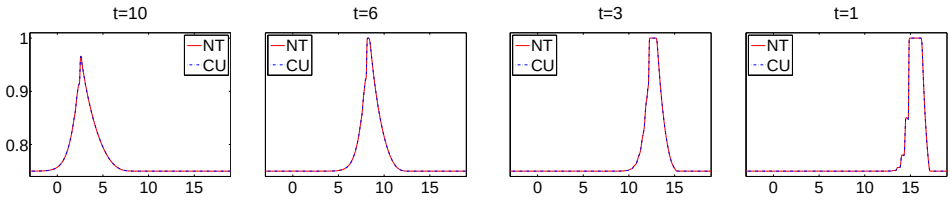

FIGURE 10. Same as in Figures 6–9 but with $\gamma = 0.5$

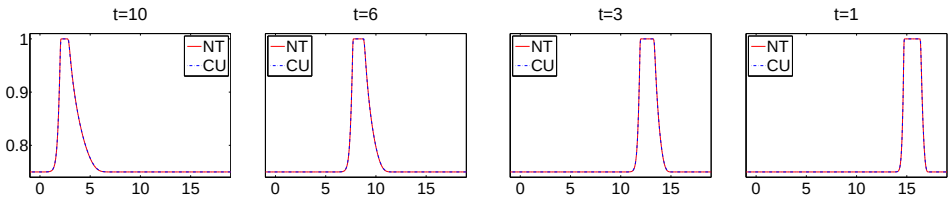

FIGURE 11. Same as in Figures 6–10 but with $\gamma = 0.1$

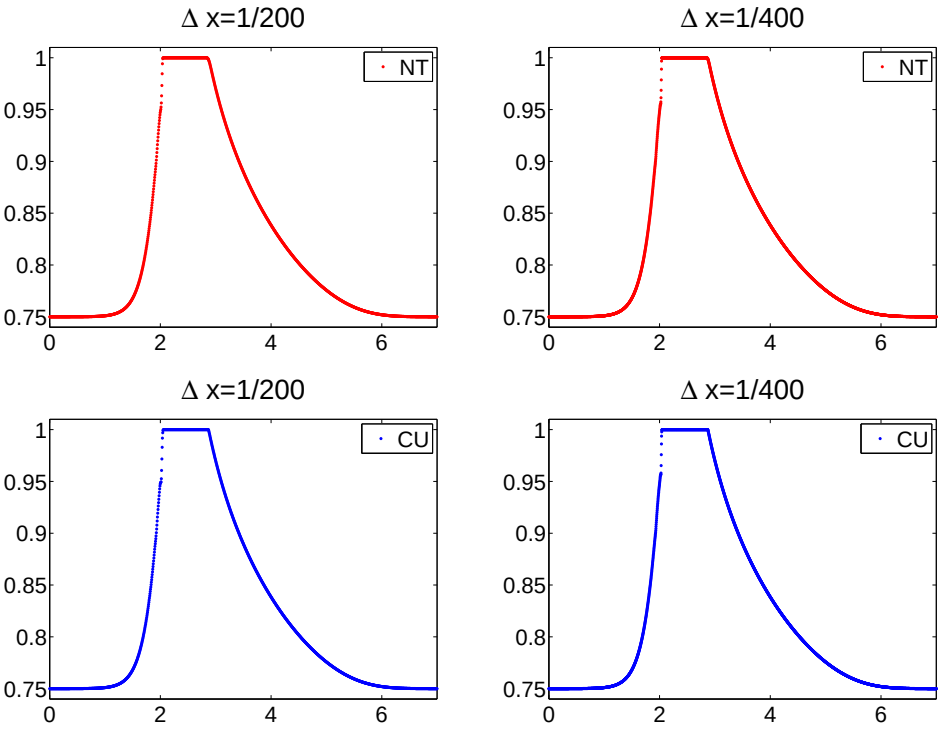

FIGURE 12. Solutions of (5), (26) with $\gamma = 0.1$ computed by the NT (upper row) and the CU (lower row) schemes at $t = 10$ on two different fine grids

2, the global flux has an apparent dispersive effect for large and intermediate values of the look-ahead parameter γ, while for small γ's a smoothing effect seems to dominate. Though a rigorous analysis of the model (5) is unavailable, the nature of the aforementioned phenomena can be heuristically explained by expanding $U(x+\gamma)$ as a Taylor series about x and rewriting equation (5) as follows:

$$u_t + \left[V_{\mathrm{m}}(u-u^2)e^{\mathrm{TS}}\right]_x = 0, \qquad \mathrm{TS} := -\left(u + \frac{\gamma}{2}u_x + \frac{\gamma^2}{6}u_{xx} + \dots\right). \tag{27}$$

Obviously, this can be done only for smooth solutions, for which (27) can be written in an equivalent nonconservative form:

$$u_t + V_{\rm m}(1-3u+u^2)e^{\rm TS}\,u_x = V_{\rm m}(u-u^2)e^{\rm TS}\left(\frac{\gamma}{2}u_{xx}+\frac{\gamma^2}{6}u_{xxx}+\ldots\right), \tag{28}$$

which suggests that for sufficiently small γ, the (nonlinear) dispersive term on the RHS of (28) is small compared to the (nonlinear) viscosity term. This leads us to a conjecture that for small γ initially smooth solutions may remain smooth for all t. However, since in this case the viscosity coefficient is also small, smooth solutions may develop sharp gradients.

To check our conjecture, we consider the following smooth initial data:

$$u(x,0) = 0.75 + 0.25e^{-(x-17)^2}, \tag{29}$$

and use the NT and CU schemes to compute the solution of the IVP (5), (29) on a uniform grid with $\Delta x = 1/80$. The final time is $t = 10$. In Figure 13, we show the solutions of this IVP for $\gamma = 0.1$ and 1. These results suggest that the solution with $\gamma = 0.1$ remains smooth, while the solution with $\gamma = 1$ seems to contain a shock discontinuity at the top part of the front. Since the strength of the shock is very low, it is quite difficult to capture numerically. A mesh refinement study, performed on two grids with $\Delta x = 1/160$ and $\Delta x = 1/320$, suggests that when $\gamma = 1$ there is a discontinuity, see Figure 14 (left) and compare it with Figure 14 (right), where a mesh refinement study of the $\gamma = 0.1$ case is performed.

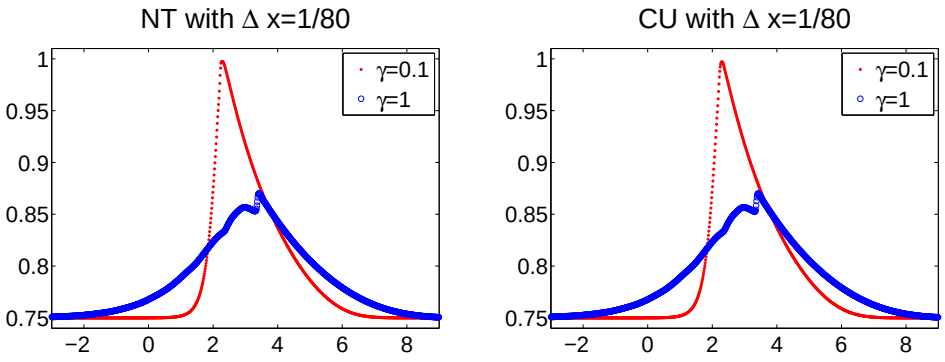

FIGURE 13. Solutions of (5), (29) with $\gamma = 0.1$ and $\gamma = 1$ computed by the NT (left) and the CU (right) schemes

In Figure 15, we demonstrate that, as expected, both the solution of the global model (5), (29) with large $\gamma = 10$ and the solution of the corresponding non-global problem (1), (29), while being very different in nature, break down in finite time.

To further validate our conjecture of a strong smoothing effect of the global flux with small γ's, we demonstrate the time evolution of the computed solution of the IVP (5), (29) with $\gamma = 0.1$, see Figure 16. As before, the grid is uniform with $\Delta x = 1/80$, and the solution does not seem to break down at any stage of its evolution. We have also performed finer grid computations (the results are not shown here) which fully support our conjecture.

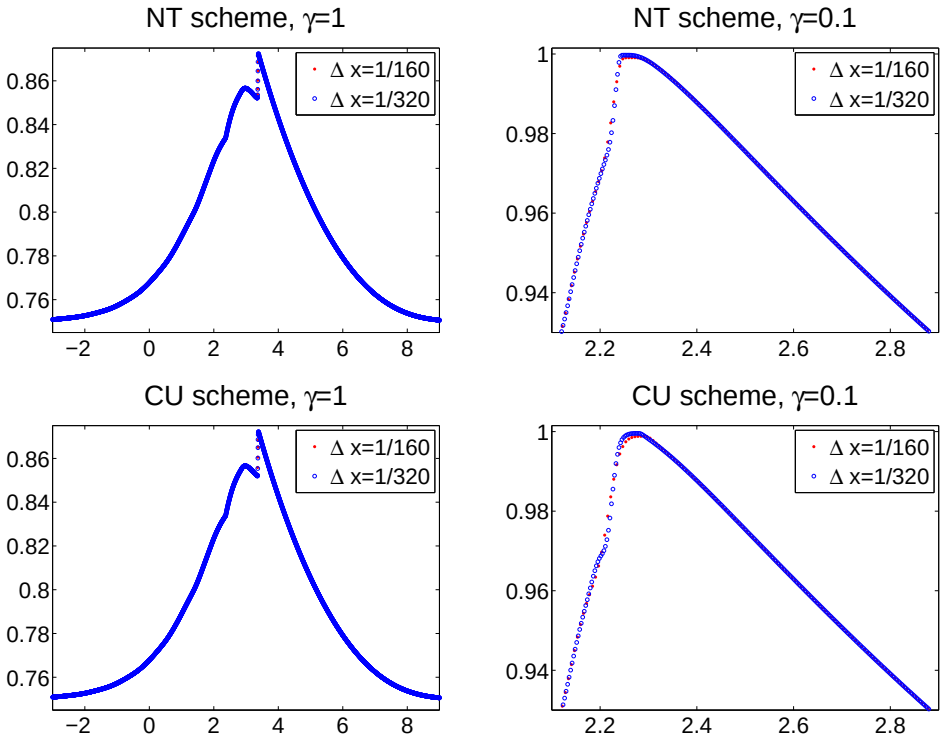

FIGURE 14. Solutions of (5), (29) with $\gamma = 1$ (left) and $\gamma = 0.1$ (right) computed by the NT (upper row) and the CU (lower row) schemes—zoom at the finer mesh results

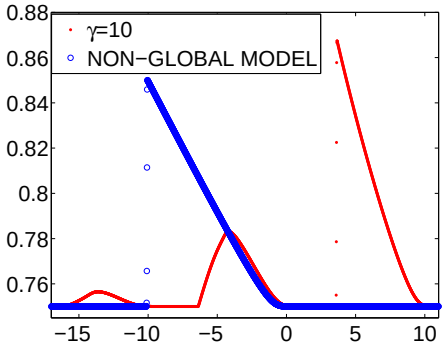

FIGURE 15. Solutions of (5), (29) with $\gamma = 10$ and of (1), (29), computed by the NT scheme

4. **Linear interaction potential.** In this last section, we consider the same "look-ahead" traffic model, but with a more realistic, linear interaction potential (6)

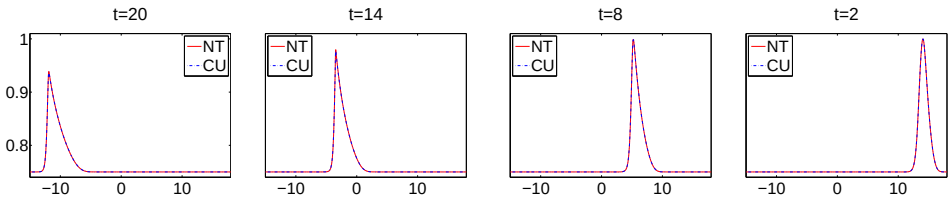

FIGURE 16. Time evolution (from right to left) of the solution of (5), (29) with $\gamma = 0.1$

instead of the constant one (4). In this case,

$$J \circ u(x,t) = \int_x^{\infty} J(y-x)u(y,t)\,dy = \frac{2}{\gamma}\int_x^{x+\gamma}\left(1-\frac{y-x}{\gamma}\right)u(y,t)\,dy.$$

Using integration by parts, the last formula can be rewritten as

$$J \circ u(x,t) = \frac{2}{\gamma}\left[\frac{1}{\gamma}\int_x^{x+\gamma} U(y,t)\,dy - U(x,t)\right]. \tag{30}$$

Note that expanding $U(y,t)$ as a Taylor series about the point $y = x + \frac{\gamma}{2}$, one obtains that for sufficiently smooth u

$$J \circ u(x,t) = \frac{U(x+\frac{\gamma}{2},t) - U(x,t)}{\frac{\gamma}{2}} + \frac{\gamma}{12}u_x(\xi(t),t), \qquad \xi(t) \in (x, x+\gamma).$$

This shows that for small look-ahead distance γ, the modified model is not expected to be much different from the original equation (5) since

$$J \circ u(x,t) \longrightarrow u(x,t) \text{ as } \gamma \to 0,$$

and hence (25) is satisfied. Indeed, when the visibility is very bad, all vehicles located within the interval $(x, x+\gamma]$ are expected to have almost the same influence on the driver of the car located at x.

However, when γ is not too small, the use of the linear interaction potential (6) is motivated by the fact that the vehicles located further away from x (but still visible to the driver there) typically have smaller influence on the driver's behavior then the vehicles that are nearby.

Formula (30) can be rewritten in a more compact form as

$$J \circ u(x,t) = \frac{2}{\gamma}\left[\frac{\mathcal{U}(x+\gamma,t) - \mathcal{U}(x,t)}{\gamma} - U(x,t)\right],$$

where $\mathcal{U}$ denotes the antiderivative of U:

$$\mathcal{U}(x,t) := \int_{-\infty}^{x} U(\xi,t)\,d\xi.$$

Using this notation, the modified version of equation (5) can be written as

$$\begin{aligned} &u_t + F(u,U,\mathcal{U})_x = 0,\\ &F(u,U,\mathcal{U}) = V_{\mathrm{m}}u(1-u)\exp\left(-\frac{2}{\gamma}\left[\frac{\mathcal{U}(x+\gamma,t) - \mathcal{U}(x,t)}{\gamma} - U(x,t)\right]\right). \end{aligned} \tag{31}$$

Though the (global) dependence of the flux F on the solution u is more complicated in (31) than in (5), the central schemes designed in §2 can be still applied after the proper modification outlined below.

First, we extend the NT scheme. The evolution formula (11) is modified according to the new global flux as follows:

$$\begin{aligned}\bar{u}^{n+1}_{j+\frac{1}{2}} &= \frac{\bar{u}_j+\bar{u}_{j+1}}{2}+\frac{\Delta x}{8}(s^n_j-s^n_{j+1})\\ &\quad -\lambda\left[F(u,U,\mathcal{U})\Big|_{(x_{j+1},\,t^{n+\frac{1}{2}})}-F(u,U,\mathcal{U})\Big|_{(x_j,\,t^{n+\frac{1}{2}})}\right].\end{aligned}\tag{32}$$

Therefore, to complete the description of the NT scheme we need to provide a recipe for the calculation of the intermediate point values $\{\mathcal{U}(x_j,t^{n+\frac{1}{2}})\}$. This can be done using the Taylor expansion with respect to t (compare with (12)):

$$\mathcal{U}(x_j,t^{n+\frac{1}{2}})\approx\mathcal{U}(x_j,t^n)+\frac{\Delta t}{2}\mathcal{U}_t(x_j,t^n).\tag{33}$$

The approximate values of $\{\mathcal{U}(x_j,t^n)\}$ can be obtained by integrating the piecewise parabolic function $\widetilde{U}^n$:

$$\mathcal{U}(x_j,t^n)=\int\limits_{x_{\min}}^{x_j}\widetilde{U}^n(\xi)\,d\xi=\Delta x\sum_{i=0}^{j-1}w^n_i+\frac{\Delta x}{2}w^n_j-\frac{(\Delta x)^2}{8}\bar{u}^n_j,\tag{34}$$

where we use the auxiliary grid variable w^n_j defined by

$$w^n_j:=\Delta x\sum_{i=0}^{j-1}\bar{u}^n_i+\frac{\Delta x}{2}\bar{u}^n_j-\frac{(\Delta x)^2}{12}s^n_j.$$

Remark 5. In principle, integrating the piecewise parabolic reconstruction $\widetilde{U}^n$, one can obtain the corresponding piecewise cubic reconstruction for $\mathcal{U}$:

$$\begin{aligned}\widetilde{\mathcal{U}}^n(x)=\int\limits_{x_{\min}}^{x}\widetilde{U}^n(\xi)\,d\xi &= \Delta x\sum_{i=0}^{j-1}w^n_i+w^n_j(x-x_{j-\frac{1}{2}})+\frac{\bar{u}^n_j}{2}(x-x_{j-\frac{1}{2}})(x-x_{j+\frac{1}{2}})\\ &\quad +\frac{s^n_j}{6}(x-x_{j-\frac{1}{2}})(x-x_j)(x-x_{j+\frac{1}{2}}),\quad x\in C_j,\end{aligned}\tag{35}$$

but if $\{x_j+\gamma\}$ are grid nodes, we only need the values of $\widetilde{\mathcal{U}}$ at the nodes $\{x_j\}$.

Finally, integrating equation (17) from $x_{\min}$ to x, we obtain

$$\mathcal{U}_t(x_j,t^n)=-\int\limits_{x_{\min}}^{x}F(u(\xi,t^n),U(\xi,t^n),\mathcal{U}(\xi,t^n))\,d\xi=:-\mathcal{F}^n_j,\tag{36}$$

where $\mathcal{F}$ is an antiderivative of F, whose point values $\mathcal{F}^n_j$ can be calculated similarly to the calculations of U^n_j in (14), namely:

$$\begin{aligned}\mathcal{F}^n_j &= \Delta x\sum_{i=0}^{j-1}F(u,U,\mathcal{U})\Big|_{(x_i,\,t^n)}+\frac{\Delta x}{2}F(u,U,\mathcal{U})\Big|_{(x_j,\,t^n)}\\ &\quad -\frac{(\Delta x)^2}{8}F_x(u,U,\mathcal{U})\Big|_{(x_j,\,t^n)}.\end{aligned}\tag{37}$$

Here, the numerical derivative F_x is calculated using, for example, the minmod limiter (16), which, together with the formulae (15) and (17), should be modified by including the dependence on $\mathcal{U}$ into the fluxes F there.

The construction of the NT scheme for equation (31) has thus been completed: the scheme is given by (32), (9), (12), (33)–(34), (15)–(17), and (36)–(37).

Next, we generalize the CU scheme for (31). It can be done in a straightforward manner, and the resulting semi-discrete scheme is (20) with the modified numerical flux given by

$$H_{j+\frac12} := \frac{a^+_{j+\frac12}F(u^-_{j+\frac12},U_{j+\frac12},\mathcal{U}_{j+\frac12}) - a^-_{j+\frac12}F(u^+_{j+\frac12},U_{j+\frac12},\mathcal{U}_{j+\frac12})}{a^+_{j+\frac12}-a^-_{j+\frac12}} + a^+_{j+\frac12}a^-_{j+\frac12}\left[\frac{u^+_{j+\frac12}-u^-_{j+\frac12}}{a^+_{j+\frac12}-a^-_{j+\frac12}} - q_{j+\frac12}\right],$$

where

$$q_{j+\frac12} = \text{minmod}\left(\frac{u^+_{j+\frac12}-u^{\text{int}}_{j+\frac12}}{a^+_{j+\frac12}-a^-_{j+\frac12}}, \frac{u^{\text{int}}_{j+\frac12}-u^-_{j+\frac12}}{a^+_{j+\frac12}-a^-_{j+\frac12}}\right),$$

$$u^{\text{int}}_{j+\frac12} = \frac{a^+_{j+\frac12}u^+_{j+\frac12} - a^-_{j+\frac12}u^-_{j+\frac12} - \left\{F(u^+_{j+\frac12},U_{j+\frac12},\mathcal{U}_{j+\frac12}) - F(u^-_{j+\frac12},U_{j+\frac12},\mathcal{U}_{j+\frac12})\right\}}{a^+_{j+\frac12}-a^-_{j+\frac12}},$$

and the flux function F is evaluated using (19), (13), and (35):

$$F(u^\pm_{j+\frac12},U_{j+\frac12},\mathcal{U}_{j+\frac12}) := V_{\text{m}}u^\pm_{j+\frac12}(1-u^\pm_{j+\frac12})\exp\left(-\frac{2}{\gamma}\left[\frac{\widetilde{\mathcal{U}}(x_{j+\frac12}+\gamma)-\widetilde{\mathcal{U}}(x_{j+\frac12})}{\gamma} - \widetilde{U}(x_{j+\frac12})\right]\right).$$

Finally, we use the developed NT and CU schemes to perform several numerical experiments to compare the new model (31) with the original one (5).

Example 4 — Traffic Jam on a Busy Freeway (Revised). We consider the same initial data (26) as in Example 2, which correspond to a traffic jam on a busy freeway, and numerically solve the IVP (31), (26) for different values of the look-ahead distance γ. We use the same grid size ($\Delta x = 1/40$) and the same set of γ's ($10, 5, 3, 1, 0.5$, and 0.1) as in Example 2. The solutions computed by the NT and CU schemes at times $t = 1, 3, 6$, and 10, are shown in Figures 17–22.

As expected, the solutions of the IVPs (31), (26) and (5), (26) are significantly different for the large values of γ ($10, 5$, and 3) and quite different for the intermediate $\gamma = 1$ — compare Figures 17–20 with Figures 6–9 for the corresponding γ's.

For $\gamma = 10, 5$, and 3, one can notice that, unlike the case of the constant interaction potential, the car density behind the traffic jam starts increasing from the very beginning — this is an effect of the linear interaction potential. As time progresses, the solutions develop dispersive wave structures, but these are less prominent and seem more realistic than the ones appearing in the solutions of the model with the constant interaction potential.

For the small γ's (0.5 and 0.1), the solutions of the model with the constant and linear interaction potentials are very similar (compare Figures 21–22 with Figures 10–11), especially at larger times.

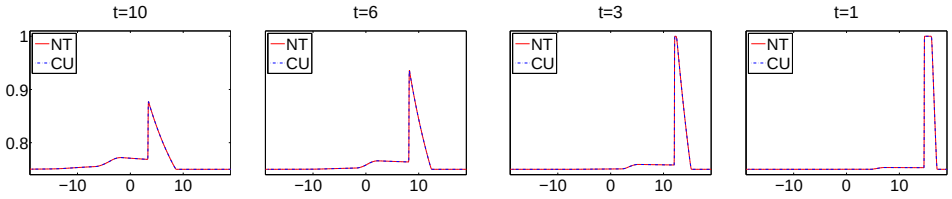

FIGURE 17. Time evolution (from right to left) of the solution of (31), (26) with $\gamma = 10$.

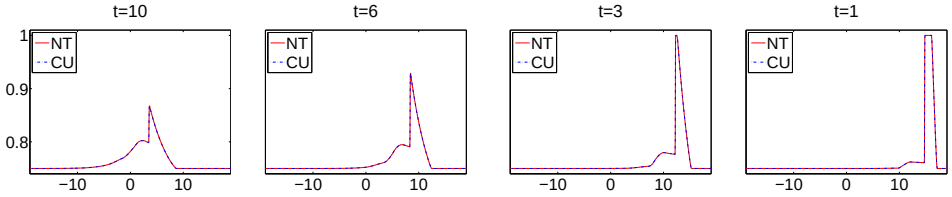

FIGURE 18. Same as in Figure 17 but with $\gamma = 5$.

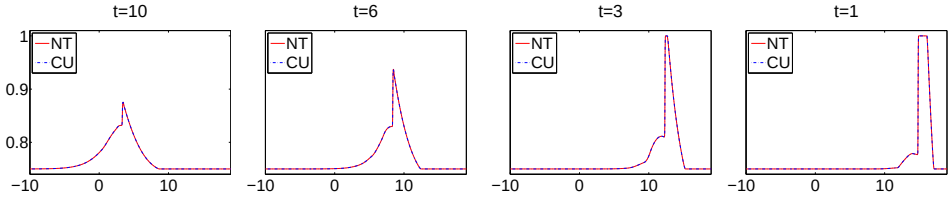

FIGURE 19. Same as in Figures 17–18 but with $\gamma = 3$.

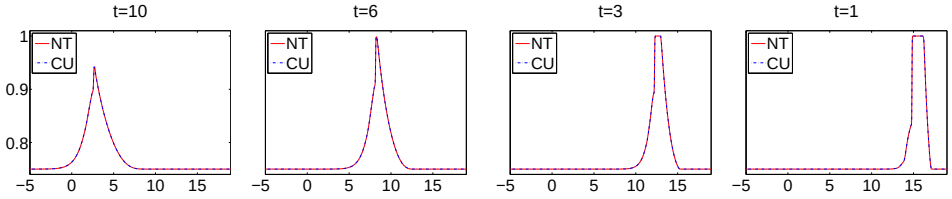

FIGURE 20. Same as in Figures 17–19 but with $\gamma = 1$.

Acknowledgments. We would like to thank the referees very much for their valuable comments and suggestions.

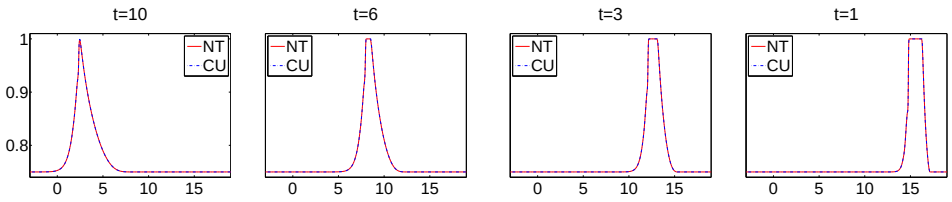

FIGURE 21. Same as in Figures 17–20 but with $\gamma = 0.5$.

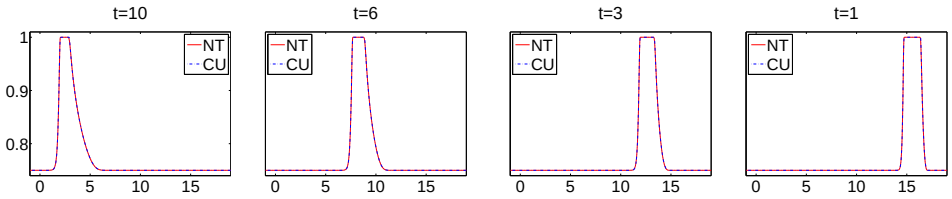

FIGURE 22. Same as in Figures 17–21 but with $\gamma = 0.1$

REFERENCES

[1] M. Bando, K. Hasebe, A. Nakayama, A. Shibata and Y. Sugiyama, *Dynamical model of traffic congestion and numerical simulation*, Phys. Rev. E, **51** (1995), 1035–1042.

[2] M. Cremer and J. Ludwig, *A fast simulation model for traffic flow on the basis of boolean operations*, Math. Comput. Simulation, **28** (1986), 297–303.

[3] K. O. Friedrichs, *Symmetric hyperbolic linear differential equations*, Comm. Pure Appl. Math., **7** (1954), 345–392.

[4] E. Godlewski and P.-A. Raviart, "Numerical Approximation of Hyperbolic Systems of Conservation Laws," Applied Mathematical Sciences, 118, Springer-Verlag, New York, 1996.

[5] S. K. Godunov, *A difference method for numerical calculation of discontinuous solutions of the equations of hydrodynamics*, Mat. Sb., **47** (1959), 271–306.

[6] S. Gottlieb, C.-W. Shu and E. Tadmor, *Strong stability-preserving high order time discretization methods*, SIAM Review, **43** (2001), 89–112 (electronic).

[7] D. Helbing, *Gas-kinetic derivation of Navier-Stokes-like traffic equations*, Phys. Rev. E, **53** (1996), 2366–2381.

[8] D. Helbing and M. Treiber, *Gas-kinetic-based traffic model explaining observed hysteretic phase transition*, Phys. Rev. Lett., **81** (1998), 3042–3045.

[9] A. Klar and R. Wegener, *Kinetic derivation of macroscopic anticipation models for vehicular traffic*, SIAM J. Appl. Math., **60** (2000), 1749–1766 (electronic).

[10] D. Kröner, "Numerical Schemes for Conservation Laws," Wiley-Teubner Series Advances in Numerical Mathematics, John Wiley & Sons, Ltd., Chichester; B. G. Teubner, Stuttgart, 1997.

[11] A. Kurganov and C.-T. Lin, *On the reduction of numerical dissipation in central-upwind schemes*, Commun. Comput. Phys., **2** (2007), 141–163.

[12] A. Kurganov, S. Noelle and G. Petrova, *Semidiscrete central-upwind scheme for hyperbolic conservation laws and Hamilton-Jacobi equations*, SIAM J. Sci. Comput., **23** (2001), 707–740 (electronic).

[13] A. Kurganov and E. Tadmor, *New high-resolution central schemes for nonlinear conservation laws and convection-diffusion equations*, J. Comput. Phys., **160** (2000), 241–282.

[14] P. D. Lax, *Weak solutions of nonlinear hyperbolic equations and their numerical computation*, Comm. Pure Appl. Math., **7** (1954), 159–193.

[15] B. van Leer, *Towards the ultimate conservative difference scheme, V. A second order sequel to Godunov's method*, J. Comput. Phys., **32** (1979), 101–136.

[16] R. LeVeque, "Finite Volume Methods for Hyperbolic Problems," Cambridge Texts in Applied Mathematics, Cambridge University Press, 2002.

[17] K.-A. Lie and S. Noelle, *On the artificial compression method for second-order nonoscillatory central difference schemes for systems of conservation laws*, SIAM J. Sci. Comput., **24** (2003), 1157–1174 (electronic).
[18] M. J. Lighthill and G. B. Whitham, *On kinematic waves. II. A theory of traffic flow on long crowded roads*, Proc. Roy. Soc. London. Ser. A, **229** (1955), 317–345.
[19] M. Muramatsu and T. Nagatani, *Soliton and kink jams in traffic flow with open boundaries*, Phys. Rev. E, **60** (1999), 180–187.
[20] K. Nagel and M. Paczuski, *Emergent traffic jams*, Phys. Rev. E, **51** (1995), 2909–2918.
[21] K. Nagel and M. Schreckenberg, *A cellular automaton model for freeway traffic*, J. Phys. I France, **2** (1992), 2221–2229.
[22] P. Nelson, *Synchronized traffic flow from a modified Lighthill-Whitman model*, Phys. Rev. E, **61** (2000), R6052–R6055.
[23] H. Nessyahu and E. Tadmor, *Nonoscillatory central differencing for hyperbolic conservation laws*, J. Comput. Phys., **87** (1990), 408–463.
[24] G. F. Newell, *Nonlinear effects in the dynamics of car flowing*, Oper. Res., **9** (1961), 209–229.
[25] P. I. Richards, *Shock waves on the highway*, Oper. Res., **4** (1956), 42–51.
[26] P. K. Sweby, *High resolution schemes using flux limiters for hyperbolic conservation laws*, SIAM J. Numer. Anal., **21** (1984), 995–1011.
[27] A. Sopasakis, *Formal asymptotic models of vehicular traffic. Model closures*, SIAM J. Appl. Math., **63** (2003), 1561–1584 (electronic).
[28] A. Sopasakis, *Stochastic noise approach to traffic flow modeling*, Phys. A, **342** (2004), 741–754.
[29] A. Sopasakis and M. A. Katsoulakis, *Stochastic modeling and simulation of traffic flow: Asymmetric single exclusion process with Arrhenius look-ahead dynamics*, SIAM J. Appl. Math., **66** (2006), 921–944 (electronic).
[30] M. Treiber, A. Hennecke and D. Helbing, *Derivation, properties, and simulation of a gas-kinetic-based, nonlocal traffic model*, Phys. Rev. E, **59** (1999), 239–253.
[31] G. B. Whitham, "Linear and Nonlinear Waves," Pure and Applied Mathematics. Wiley-Interscience [John Wiley & Sons], New York-London-Sydney, 1974.

Received April 2008; revised February 2009.

E-mail address: kurganov@math.tulane.edu
E-mail address: apolizz@tulane.edu